ISTITUTO NAZIONALE DI RICERCA METROLOGICA
Repository Istituzionale

Magnetic metal-ceramic nanocomposites obtained from cation-exchanged zeolite by heat treatment in reducing atmosphere

(Article begins on next page)

03 May 2024

Magnetic metal-ceramic nanocomposites obtained from zeolite precursors by means of a smart (and scalable) process

Serena Esposito[1], Gianfranco Dell'Agli[1], Antonello Marocco[1], Barbara Bonelli[2], Paolo Allia[2], Paola Tiberto[3], Gabriele Barrera[3*], Maela Manzoli[4], Rossella Arletti[5], Michele Pansini[1*]

[1]Department of Civil and Mechanical Engineering and INSTM Research Unit, Università degli Studi di Cassino e del Lazio Meridionale, Via G. Di Biasio 43, 03043 Cassino, FR, Italy.

[2]Department of Applied Science and Technology and INSTM Unit of Torino-Politecnico, Politecnico di Torino, Corso Duca degli Abruzzi 24, 10129 Torino, Italy.

[3]INRIM, Nanoscience and Materials Division, Strada delle Cacce 91, 10135 Torino, Italy.

[4]Department of Drug Science and Technology, Università degli Studi di Torino, Via Pietro Giuria 9, Torino, Italy.

[5]Dipartimento di Scienze della Terra, Università degli Studi di Torino, Via Valperga Caluso, 35, 10125 Torino, Italy.

*Michele Pansini, Department of Civil and Mechanical Engineering, Università degli Studi di Cassino e del Lazio Meridionale, Via G. Di Biasio 43, 03043 Cassino (FR), Italy.

E-Mail: pansini@unicas.it

1

ABSTRACT

Magnetic nanocomposites are highly demanded on account of their multifarious applications in many technological fields, as they can be easily separated from the media where they are used.

Here, we report a smart (and scalable) process to produce magnetic metal-ceramic nanocomposites formed by Ni^0 nanoparticles (5-25 nm) dispersed in an amorphous silica-alumina matrix.

Nanocomposites were obtained from Ni^{2+} exchanged A and X zeolites by means of a two-steps process encompassing: 1) ion exchange of commercial zeolites; 2) thermal treatment (735-750 °C) in reducing atmosphere.

Obtained nanocomposites were characterized by means of atomic absorption spectrometry, thermal techniques (themogravimetry, differential thermal analysis and temperature programmed reduction), X-rays powder diffraction (with synchrotron source) followed by Rietveld analysis, High Resolution Transmission Electron Microscopy, N_2 adsorption/desorption at -196 °C and magnetic measurements at both room temperature and low temperature.

Physico-chemical characterization of the nanocomposites allowed evidencing some of their peculiar properties such as: the different extent of Ni^{2+} reduction to Ni^0 in nanocomposites obtained from the two zeolites, the dimensions of the resulting metal nanoparticles, the textural and compositional properties of the matrix embedding the Ni^0 nanoparticles.

The results of this work show that the properties of the nanocomposites, final product of the process here proposed, can be tailored by a wise choice of the parent zeolite, which markedly affects their morphology, and by properly tuning the thermal treatment conditions, *i.e.* temperature and time.

Keywords: magnetic nanocomposites, zeolite precursors, metal-ceramic nanocomposites

2

1. INTRODUCTION

In the last two decades, the use of nanoparticles/nanomaterials has revolutionized the scenario of current technologies, since nanosized materials have markedly different properties from their bulk analogues, mainly due to the large difference in surface area and surface energy [1,2].

As far as nanoparticles (NPs) and nanomaterials bearing a technological impact are concerned, magnetic NPs are attracting growing interest for several reasons, including the simple separation from the *media* in which they are used [2,3]. Indeed, several magnetic NPs are used in the fields of magnetic fluidics [4]; catalysis and adsorption [5,6]; biotechnology/biomedicine [7]; magnetic resonance imaging [8,9]; data storage [10] and environmental remediation [11,12].

Their use is often limited by the natural tendency of NPs to form aggregates/agglomerates in order to minimize their surface energy. Moreover, unprotected metal NPs are easily oxidized in air, with a consequent loss of dispersibility and of magnetic properties. Thus, for many applications, it is of crucial importance to be able to protect magnetic NPs against several degradation processes (agglomeration/aggregation/oxidation) occurring both during and after synthesis.

Therefore, magnetic NPs are generally used under the form of two types of nanocomposites (NCs): either the magnetic component is the nanoparticle core, which is encapsulated by a shell of matrix material, [3] or the magnetic component is evenly dispersed in a matrix material [3].

The most common methods to synthesize stable magnetic NPs include sol-gel assisted co-precipitation; thermal decomposition; micro-emulsion; hydrothermal synthesis; gas phase deposition; electron beam lithography; sonochemical synthesis and hydrolysis [1,13-15]. Though powerful and versatile, those techniques require complicated procedures and lengthy operations, which must be carried out by well-experienced scientists: indeed, they may provide fair results at a laboratory scale, but are hardly suitable for large scale productions. This, along with the need of expensive reactants, leads to high cost of the final product.

Finding a method to produce higher amount of NCs with tailored properties could expand their use: previous studies [1,10,14] clearly indicated the demand for moderate (or low) cost, simple and effective procedures for the preparation of magnetic NCs, with high performances in various technological sectors.

To this respect, some of us [16,17] patented a smart process to obtain magnetic NCs from commercial zeolites [18,19]. The process envisages two steps, *i.e.* an ionic exchange of the zeolite with a heavy metal (Ni, Fe or Co) and a thermal treatment at relatively mild temperature (500-850 °C) under reducing atmosphere, obtained by flowing a 2.0 vol. % H_2 in Ar mixture.

The obtained materials belong to the second type of magnetic NCs previously described, where the magnetic component is evenly dispersed in a matrix stemming from the zeolite collapse.

The physico-chemical properties of the final NCs markedly differ from those of the parent zeolite, though they may exhibit a residual (irregular) porosity, which is the only remnant of the parent zeolite structure and which can have an impact on the ultimate technological application.

The main goal of the present study is to describe the unique physico-chemical properties of two sets of magnetic NCs obtained from Ni^{2+} exchanged A and X (commercial) zeolites. The process is indeed versatile, in that other exchange metals (like Fe and Co) and other zeolites can be used, as reported in our previous works [16,17,20,21]. Here, the choice of A and X zeolites was dictated by their high cation exchange capacity due to their Si/Al ratio (1.00 and 1.23, respectively), as well as by their low cost (related to their widespread use in many technological areas) [22,23].

Moreover, the process has the characteristics of a scalable method, in that it implies an ionic exchange and a thermal treatment under gas flow.

The so-obtained NCs were characterized by means of several techniques, with the aim of assessing some (technologically relevant) physico-chemical properties, like the extent of Ni^{2+} exchange; the extent of Ni^{2+} reduction to Ni^0; the size of Ni^0 NPs; the morphology of the final NCs and their magnetic behavior.

4

2. EXPERIMENTAL SECTION

2.1 Synthesis of the nanocomposites

Carlo Erba reagent grade synthetic 4A zeolite (framework type LTA, $Na_{12}Al_{12}Si_{12}O_{48}\cdot27H_2O$, hereafter referred to as "A zeolite") and 13X zeolite (framework type FAU, $Na_{86}Al_{86}Si_{106}O_{384}\cdot264H_2O$, hereafter referred to as "X zeolite") were used. Exchange solutions were prepared dissolving Carlo Erba reagent grade 99.5 wt.% $NiCl_2\cdot6H_2O$, nickel(II) chloride hexahydrate, in doubly distilled water. Their experimental cation exchange capacity (as determined by the "batch exchange method") [24,25] was very close to the calculated cation exchange capacity of 5.48 and 4.73 $meqg^{-1}$ for A and X zeolite, respectively.

The parent A and X zeolites were contacted with a $[Ni^{2+}]$ = 0.2 M solution with a solid/liquid weight ratio of 1/20 and contact time (t) = 2 h at 70 °C. The initial pH of the exchange solution was 6.6; the pH of the exchange solution-zeolite suspensions was 7.0 (A zeolite) and 6.7 (X zeolite).

The solid was separated from the liquid by filtration and contacted again with a fresh solution: this step was repeated ten (A zeolite) or six (X zeolite) times, based on the different exchange capacity of the two zeolites [18,19].

The resulting powders were washed with doubly distilled water, dried for about one day at 80 °C, and stored for at least 3 days in an environment with about 50% relative humidity to allow water saturation of the zeolite.

Three aliquots of each Ni^{2+} exchanged zeolite (both NiA and NiX) were subjected to the following thermal treatments under reducing atmosphere (*i.e.* a flow of a gaseous mixture containing 2 vol. % H_2 in Ar) in an alumina tubular furnace (inner diameter = 6.9 cm, height = 91 cm), using Pt crucibles. Two temperatures of treatment, *i.e.* 735 and 750 °C, were selected based on thermos gravimetric analysis carried out under the same reducing atmosphere, showing an almost total zeolite structure collapse above 700 °C (*vide infra*):

5

1) NiA735C-12min and NiX735C-12min samples were obtained by heating from r.t. to 735 °C (15 °C min^{-1} heating rate) and a subsequent isothermal step at 735 °C for 12 min. The heating system of the furnace was then switched off and the sample left to cool down to r.t. within the furnace.

2) NiA750C-12min and NiX750C-12min samples were obtained by heating from r.t. up to 750 °C (15 °C min^{-1} heating rate) and a subsequent isothermal step at 750 °C for 12 min. The heating system of the furnace was then switched off and the sample left to cool down to room temperature within the furnace.

3) NiA750C-0min and NiX750C-0min samples were obtained by heating from r.t. up to 750 °C (15 °C min^{-1} heating rate) and then by switching off the heating system as soon as the temperature of 750 °C was reached. The samples were left to cool down to r.t. within the furnace.

2.2 Methods

The Ni^{2+} and (residual) Na$^+$ contents of NiA and NiX zeolites were determined by dissolving the zeolite in a HF and HClO$_4$ solution and by determining the Ni^{2+} and Na$^+$ contents by means of atomic absorption spectrophotometry (AAS, Perkin-Elmer Analyst 100 apparatus) [26,27].

The parent A and X zeolites and the Ni-exchanged ones were characterized by X-ray powder diffraction (XRPD) on a Philips X'Pert diffractometer equipped with a Cu K$_\alpha$ radiation (2θ range = 5° - 100°; step = 0.02° 2θ; time per step = 1 s) [28,29].

Quantitative phase analysis (QPA) of the NCs was performed by using synchrotron radiation XRPD (experiments performed on the high-resolution beamline ID22 at ESRF (Grenoble), with a fixed wavelength of 0.413278 Å). NCs powders were packed along with Al$_2$O$_3$ (10 wt. %) as internal standard in a boron capillary and spun under the beam; the diffraction patterns were collected using a 2D detector Perkin Elmer XRD 1611CP3. The combined RIR-Rietveld method, which enables the

QPA and the calculation of both the crystalline and amorphous fractions [30] was performed by using the GSAS package [31] with the EXPGUI interface [32].

Simultaneous differential thermal analysis (DTA) and thermogravimetric analysis (TGA) were performed under a reducing atmosphere, obtained by a flow of H_2-Ar gaseous mixture (2 vol. % H_2), using a Netzsch thermoanalyser model STA 409, α-Al_2O_3 as reference, and a 10 °C min^{-1} heating rate.

Temperature Programmed Reduction (TPR) measurements were carried out in a laboratory flow apparatus, using a 5 vol. % H_2 in Ar ($Q = 20\ cm^3 min^{-1}$) with heating rate of $10°$ C min^{-1} from r.t. to 800 °C. The sample (*ca.* 100 mg) was loaded in a quartz down-flow cell with a K thermocouple in close contact with the sample.

N_2 adsorption/desorption isotherms at −196 °C were obtained with a Quantachrome Autosorb 1 instrument on samples previously outgassed at 250 °C for 4h to remove water and other atmospheric contaminants. The specific surface area of the samples was calculated according to the Brunauer–Emmett–Teller (BET) method (S_{BET}) [33]. The total pore volume (V_p) was determined from the amount of adsorbed N_2 at $P/P_0 = 0.98$; both the micropore volume and external surface area were calculated according to the *t*-plot method. The pore size distribution (PSD) was calculated by using the non-local density functional theory (NL-DFT) method from the isotherms adsorption branches by applying a N_2-silica kernel.

Transmission electron microscopy (TEM) and high resolution TEM (HR-TEM) analyses of the NCs were carried out with a JEOL 3010-UHR instrument operating at 300 kV and equipped with a LaB_6 filament. Digital micrographs were acquired by a (2k x 2k)-pixel Ultrascan 1000 CCD camera and processed by Gatan digital micrograph. Before the measurements, to obtain a good dispersion of the sample particles and avoid any modification induced by the use of a solvent, the powders were briefly contacted with the lacey carbon Cu grids, resulting in the adhesion of some particles to the sample holder by mere electrostatic interactions. Histograms of the particle size distribution were obtained by considering *ca.* 300 particles on the TEM images, and the mean particle diameter (d_m)

was calculated as $d_m = \Sigma d_i n_i / \Sigma n_i$, where n_i was the number of particles of diameter d_i. The counting was performed on electron micrographs obtained starting from 30,000 magnifications, where Ni particles, well contrasted with respect to the amorphous decomposed zeolite matrix, were clearly observed. It is worth noting that mainly small NPs (with average diameter <15 nm) were observed, whilst the presence of very few metallic particles with larger size (average diameter >50 nm) was detected. However, the number was too low to be considered as representative of the morphology of the samples.

The magnetic properties of the NCs were studied at both r.t. and 5 K (low T) by using a SQUID magnetometer operating in the 0-70 kOe range. The FC/ZFC curves of Ni-rich zeolites were obtained under a field of 200 Oe in the temperature interval 10-300 K using the Lakeshore VSM.

3. RESULTS and DISCUSSION

3.1 Chemical Composition and XRD patterns of NiA and NiX zeolites

According to AAS chemical analysis, the NiA sample contains 4.11 meq g^{-1} Ni^{2+} and 1.37 meq g^{-1} Na^+, and the NiX sample contains 3.73 meq g^{-1} Ni^{2+} and 1.00 meq g^{-1} Na^+. The corresponding cation equivalent fractions were calculated of $x_{Ni} = 0.75$ and $x_{Na} = 0.25$ (NiA sample), and $x_{Ni} = 0.79$ and $x_{Na} = 0.21$ (NiX sample).

The weight percentage of Ni (wt. % Ni) in the final NCs, calculated on the basis of the Ni^{2+} content of the exchanged zeolites by considering the final NCs as completely dehydrated materials, was 15.0 and 14.4 wt.% Ni in NCs derived from NiA and NiX, respectively.

The XRD patterns of the parent A and X zeolites and of the NiA and NiX samples are reported in Electronic Supplementary Material (ESM), Fig. S1. Their examination reveals that the intensity of most of the diffraction peaks of the two zeolites is depressed by Ni^{2+} exchange. Nonetheless, the intensity of some minor diffraction peaks of the two zeolites turns out strengthened by Ni^{2+} exchange. These findings may be reasonably interpreted on the basis of a distortion of the zeolite

8

framework upon Ni^{2+} exchange. This distortion is more evident with the A zeolite than with the X zeolite.

3.2 Thermal characterization and Quantitative Phase Analysis

TG analysis and DTA under 2 vol. % H_2 in Ar reported in Fig. 1a (NiA) and 1b (NiX) showed different phenomena occurring with the two samples.

The NiA sample lost *ca.* 29 wt. %: a 20 wt.% loss occurred in the 28 – 260 °C range, due to dehydration, whereas the mass loss between 260 and 700 °C was 9 wt.% (Fig. 1a). According to TG analysis, the structure collapse is almost complete above 700 °C. As reported in the literature, NiA zeolites with comparable Ni^{2+} content show a similar wt. % loss during TG analysis (28-29 wt.%), mainly ascribed to dehydration [34]. The DTA curve of the NiA sample (Fig. 1a) shows an endothermic peak in correspondence of dehydration, whereas a broad exothermic signal is observed above 260 °C, with a maximum at 480 °C, likely due to the collapse of the zeolite crystalline structure.

With NiX sample, the total mass loss during TG analysis was 33 wt. %, and occurred in a wider range of temperature from r.t. to *ca.* 750 °C. According to the literature [35], Ni^{2+} exchange brings about a loss of stability on X zeolite: NaX becomes amorphous above 930 °C, whereas NiX zeolites start collapsing below 800°C, depending on the degree of ionic exchange, and keep losing water in a wider range of temperature, the water being due to the hydration sphere of exchanged Ni^{2+} ions. The TG curve of the NiX sample is in agreement with those reported in literature, in that the mass loss continues as the temperature increases, and different mass losses at ca. 60, 190 and 475 °C are observed, due to dehydration of hydrated Ni^{2+} ions. The DTA curve (Fig. 1b) shows an endothermic signal below 270 °C and then a broad and structured exothermic signal with maxima at 390, 510 and 630 °C assigned to several steps of zeolite collapse. Comparison with the literature is feasible only from the qualitative point of view, since several factors including heating rate, temperature ramp, type of gas and sample size affect the temperatures at which exothermic peaks are observed.

9

Here, the presence of H_2 in the gas flow brings about the reduction of Ni^{2+} species along with thermal collapse of the zeolite crystalline structure. As a whole, the reported TG and DTA curves show that the NiX sample is less thermally stable with respect to the NiA sample.

The XRDP patterns of NiA-derived NCs and of NiX-derived NCs are reported in Fig. 2 and 3, respectively. Those patterns were used to obtain the QPA results reported in Table 1.

In both series of samples, a low amount of crystalline phases is present in the amorphous matrix (representing~80 wt. % of all the investigated compounds): among those crystalline phases, it is possible to recognize the precursor zeolite.

With NiX-derived NCs, the crystalline precursor is present at levels lower than 0.5%, indicating an almost total destruction of the structure, whereas a higher amount of pristine NiA zeolite is found in the corresponding NCs, in agreement with TG analysis.

As a whole, the QPAs indicate more homogenous phase compositions for the NiX-derived NCs, which, independently from the heat treatment, show the same phase quantitative composition. Metallic Ni (Ni^0) peaks were observed in all the patterns and the QPA indicates and amount of Ni^0 ranging from 4 to 7.5 wt. % in NiA-derived NCs, and around 10 wt. % in NiX-derived NCs, respectively. In almost all the samples (with the exception of Ni-A750C-12min sample) broad peaks attributable to nano-crystalline NiO (bunsenite structure) were detected, though in different amounts, always higher in NiX-derived NCs (~5-6% vs. ~1% in NiA-derived NCs).

A further Ni-bearing phase, specifically a nickel hydride (HNi_2) with hexagonal structure, was detected only with NiA-derived NCs [36]. The HNi_2 phase shows broad peaks, indicating a very low degree of crystallinity. It is present in amount ranging from ~1 to ~4 wt.%, the highest amount being found in the sample treated at higher temperature for longer time, which is, by the way, the NiO-free sample (NiA750C-12min).

During Ni^{2+} exchange some NiO likely forms, which undergoes reduction to a different extent, depending on the type of pristine zeolite (either NiA or NiX). Data in Table 1 show that, as a whole, in NiA-derived NCs *ca.* 60 % of Ni^{2+} was reduced, and the remaining 40 % was mainly found in the

10

amorphous phase, whereas in NiX-derived NCs *ca.* 67 % of all the Ni^{2+} species were reduced, the remaining Ni^{2+} species being found mostly in the NiO phase.

In order to get a greater insight into the reduction behavior of Ni^{2+} cations, TPR analysis was performed on both NiA and NiX zeolites. The TPR profiles (not reported) showed several reduction peaks for both samples in the 500-800 °C temperature range. The corresponding amount of consumed H_2 was 10053.23 $\mu molg^{-1}$ for NiA zeolite and 1750.19 $\mu molg^{-1}$ for NiX zeolite. Simple stoichiometric calculations made by considering the nickel wt. % in the dehydrated zeolites and the H_2/Ni^{2+} molar ratio showed that the NiA zeolite consumed *ca.* 4 times the amount of H_2 needed for the whole reduction of the Ni^{2+} species. This result is in agreement with both the low amount of NiO phase and the presence of HNi_2 in NiA-derived NCs, indicating the likely occurrence of a spillover effect in this set of samples [37].

Moreover, the sample with the highest amount of HNi_2 was NiA750C-12min, where both the high T and the longer reaction time allow the decomposition of the hydride. *Vice versa*, NiX consumed an amount of H_2 slightly below the stoichiometric amount, in agreement with the presence of a higher wt.% of NiO and the absence of HNi_2 in the final NCs.

3.3 Textural and Morphological Characterization

N_2 adsorption isotherms at -196 °C of the NCs (reported in ESM, Fig. S2) are of type II, as proper of either non-porous adsorbents or adsorbents having relatively large pores, and show H3 type hysteresis loops, associated with the presence of slit pores [38]. The adsorption isotherms were used to determine the values of specific surface area (S_{BET}), the total pore volume (V_p), the micropore volume (V_{mp}) reported in Table 2, showing that the zeolite collapse brought about a densification phenomenon, leading to low surface area NCs. The pore size distribution (PSD) curves (Fig. 4) evidenced a remarkable difference between the two sets of NCs deriving by the two zeolites: a non-negligible fraction of micropores, resembling the ones characteristic of the zeolite structure, is still present in NiA-derived NCs, in agreement with the higher content of residual NiA zeolite measured

11

by QPA (Table 1). In addition, NiA thermal collapse brought about also the formation of mesopores with a diameter size below 10 nm. NiX-derived NCs, instead, showed an irregular distribution of mesopores, including both smaller mesopores (with a diameter below 12 nm, more abundant) and larger mesopores (with a diameter in the 12 – 50 nm range, less abundant).

As a whole, the results stemming from the analysis of N_2 adsorption at -196 °C show that the type of parent zeolite affects the porosity of the final NCs, in that NiX leads to materials with a very disordered mesoporosity, Fig. 4.

An extended TEM and HR-TEM characterization was carried out on all the obtained samples in order to get insights on the morphology of the synthesized materials as well as on the Ni particle size and on the crystalline habit. A selection of TEM and HR-TEM micrographs was shown in Figs. 5, 6 and 7 (for samples NiA735C-12min, NiA750C-0min and NiX735C-12min, respectively).

With the NiA735C-12min sample, the thermal treatment at high temperature produced large particle agglomerates with square shape (Fig. 5a) that are made up of small crystalline Ni^0 NPs (Fig. 5b) embedded into an amorphous matrix, resulting from the decomposition of the NiA zeolite (Fig. 5c). The analysis of the observed diffraction fringes (as that reported in Fig. 5d) as well as of the Fourier Transform of all the high resolution images (see, for example, Fig. 5e) showed that those NPs expose the (200) and (220) faces of cubic Ni^0 (JCPDS file number 00-001-1258), in agreement with the XRDP findings. The particle size distribution of the Ni^0 NPs ranges between 5 and 40 nm, resulting in a mean diameter equal to 17.6 ± 5.8 nm (Fig. 8).

An increase of the temperature from 735 up to 750 °C during the synthesis (NiA750C-12min sample, the corresponding TEM and HR-TEM micrographs being reported in Fig. S3 of the ESM) produced no significant changes in the overall morphology of the obtained material, except for the size of the Ni^0 NPs. Indeed, as shown in Fig.8, the particle size distribution becomes broader and the average diameter is of 22.1 ± 8.0 nm. This feature clearly indicates that a temperature increase from 735 up to 750 °C, though limited, favoured the agglomeration of the Ni^0 NPs into larger ones.

12

Interestingly, with the NiA750C-0min sample (Fig. 6), for which the heating system was switched off as soon as the temperature of 750 °C was reached, the obtained average diameter of the Ni^0 NPs is 16.7 ± 4.2 nm, with the narrowest particle size distribution ranging between 5 and 30 nm (Fig. 8). If compared to the other two materials obtained from the NiA zeolite, the morphology of the NiA750C-0min sample looks similar. However, the material is made up of large particle agglomerates with square shape (Fig. 6a and 6b), where small crystalline Ni^0 NPs with homogeneous globular form and size are enveloped in an amorphous frame (Fig. 6b and 6c). It was found that the Ni^0 NPs expose the (111) face of the Ni^0 cubic phase (JCPDS file number 00-001-1258) as confirmed by the distances among the diffraction fringes (Fig. 6d) and by the analysis of the Fourier Transform of the images (Fig. 6e). Therefore, the synthetic procedure allowed obtaining a uniform material in which nucleation, rather than growth, was favoured by the instantaneous drop of the temperature at 750 °C.

A totally different morphology was observed with NiX-derived NCs: large particle agglomerates with globular shape were detected (sample NiX735C-12min, Fig.7a). Moreover, the observation at higher magnification put in evidence agglomerates with a hedgehog morphology, in which needles decorated by small roundish Ni^0 NPs embedded into an amorphous matrix can be recognized, as shown in Fig. 7b. The Ni^0 NPs have quite uniform size, as indicated by the narrow particle size distribution reported in Fig. 8, with an average size of 12.7 ± 3.7 nm and expose the (200) and (111) faces of cubic Ni^0 (JCPDS file number 00-001-1258), as confirmed by the distances among the diffraction fringes of particle 1 and particle 2 shown in Fig. 7c.

Independently from both temperature and time of the thermal treatment, the hedgehog-like morphology is common to all the NiX-derived NCs, as shown in Figs. S4 and S5 in the Electronic Supplementary Material for the NiX750C-12min and NiX750C-0min samples, respectively. In addition, small differences concerning the particle size distributions and the average diameters of the Ni^0 NPs have been found (12.5 ± 3.4 nm for NiX750C-12min and 13.5 ± 3.6 nm for NiX750C-0min). Therefore, the TEM findings indicated that, at variance with what observed in the case of

13

NiA-derived NCs, the use of NiX zeolite as a precursor allowed obtaining Ni^0 NPs with homogeneous size around 13 nm, as illustrated in Fig. 8. Interestingly, the NiX750C-12min sample is the material possessing the narrowest particle size distribution, indicating that the thermal treatment at 750 °C for 12 min has a beneficial effect on the homogeneity of the Ni^0 NPs size.

3.4 Magnetic Characterization

The saturation magnetization M_s (H=70 kOe) of all the NCs is reported in Fig. 9a. The values of M_s in NiX-derived NCs are somewhat higher than the corresponding values in NiA-derived ones. In both sets, the highest M_s is found for a reaction temperature of 750°C and for a reaction time of 12 min. The measured values of M_s, which range between 2.82 and 4.07 emu g^{-1}, are in notable agreement with the data of Table 1 when the fraction of hexagonal nickel hydride HNi_2 is properly taken into account, as shown in Fig. 9b. This implies that the HNi_2 phase carries a magnetic moment per Ni atom comparable with that of metallic Ni^0. As known [S. Araújo-Barbosa, M.A. Morales, Journal of Magnetism and Magnetic Materials 441 (2017) 702–709, and references therein] the magnetic behavior of Ni hydrides is strongly dependent on the [H]/[Ni] ratio; in particular, a ferromagnetic (α-NiH) and a nonmagnetic (β-NiH) phase coexist in bulk samples of partially hydrogenated nickel. On the other hand, nickel hydride nanoparticles are characterized by a ferromagnetic phase even at high H concentrations ([H]/[Ni] → 1)   [Barbosa]. In line with these results, Fig. 9b suggests that the HNi_2 phase observed in our nanocomposites must be characterized by a predominant ferromagnetic behavior which adds to the contribution from the Ni^0 phase.

The r.t. coercivity of all examined samples is shown in Fig. 10. The coercivity is higher in NiA-derived NCs with respect to those derived from NiX; the maximum H_c is found with NiA750C-12min sample and with NiX750C-0min sample. The different behavior observed for H_c in the two materials reflects more the differences among nanoparticle size distributions (Fig. 8) than the structural differences between the precursor zeolites. A higher coercivity is expected in

14

In order to ascertain the type and extent of aggregation of the magnetic fraction embedded in the diamagnetic host, FC/ZFC low-field magnetization was measured in all the samples; two representative FC/ZFC curves taken between 10 K and r.t. are shown in Fig. 11 for both types of NCs; the curves of all samples are basically the same as the ones shown here for two representative samples (NiA750C-12min and NiX750C-12min). The shape of the curves indicates that the mean NPs size is well above 10 nm, in agreement with TEM observations, and that the NPs can be magnetically interacting, although the TEM image do not provide enough support for predominant contact interactions. The measured coercivity is typical of nanometer-sized ferromagnetic particles; the lower H_c values found in NiX derived NCs could point to a weaker interparticle coupling.

Representative magnetic loops at 5 K in two selected samples (NiA735C-12min and NiX735C-12min) are reported in Fig. 12 together with the corresponding loops measured at r.t.. All the samples display a similar behavior: at r.t., magnetic saturation is quickly reached (at about 4000 Oe), while the low-temperature curves show a huge non-saturating effect with a small negative concavity. The M(H) curves measured at 300 K are well fitted by a Langevin function with a magnetic moment corresponding to the mean value expected by using the histograms of Fig. 8 (an example is reported in Fig. 12, inset of bottom panel). This result suggests that the interparticle coupling is not very strong, and that the NPs are still individually responding to the applied field.

Starting from the FC/ZFC curves it is possible to independently estimate the distribution of NPs sizes from magnetic data (see ref. [39] for explicit formulas), under the hypothesis that the NPs are basically non-interacting. An example of this procedure for sample NiX735C-12min is shown in Fig. 8, upper right panel, where the p(D) distribution obtained from magnetic data (full symbols) using a temperature-dependent anisotropy K(T) is superimposed to the histogram obtained from TEM image analysis. Considering the size of the NPs under study, a K(T) curve appropriate to bulk

15

Ni^0 has been used [40]. The agreement between the two sets is fairly good, again pointing to a weak interparticle interaction.

The low temperature non-saturating effect, which completely disappears at r.t., indicates the presence of a non-negligible fraction of Ni which does not participate in the standard nanoparticulate phase. The isolated Ni fraction can be related to the presence of either very small Ni clusters (typical diameter: $\cong$ 1 nm) or paramagnetic Ni^{2+} ions; however, even small magnetic clusters should give a detectable contribution to the M(H) curve at very large fields even at room temperature, which is not the case (Fig. 12). Therefore, the magnetic measurements confirm that in addition to the nanoparticulate Ni^0 phase the host material contains a non-negligible fraction of either Ni^{2+} ions or Ni atoms, genuinely paramagnetic at r.t., whose contribution to the M(H) curve is therefore expected to be negligible even under fields as large as 70 kOe. Such cations can belong either in the NiO$_x$ compound(s) found by the RIR-Rietveld analysis of X-ray patterns (see Table 1), which mostly occur in NiX-derived NCs, or in the fraction of residual zeolite, which mostly occurs in NiA-derived NCs; in this case, the cations may occur as substitutional ions [41], or in other complexes exhibiting a paramagnetic phase at high temperature [42], or can be present as basically isolated Ni^{2+} cations dispersed in the host structure and cavities [42].

The present measurements cannot provide a further insight on the nature of meso- or nanostructures containing Ni^{2+} ions in the materials under study; in particular, no information about the type of magnetic ordering of moments on Ni^{2+} ions at low temperatures (typically, below 10 K) can be obtained, so far. The interpretation of magnetic data about the paramagnetic phase is strongly hindered by the presence of the dominant signal from the Ni^0/HNi$_2$ NPs. Further measurements, involving a detailed analysis of the magnetic response of all materials at very low temperatures would be needed. On the other hand, the presence of a significant fraction of paramagnetic Ni^{2+} cations dispersed in the zeolite cage explains the relatively low vales of M$_s$ measured at r.t. in all the samples (Fig. 9). A zeolite containing 15 wt. % Ni^0 should exhibit a M$_s$ of about 8.6 emu g^{-1} in a diamagnetic host containing 15 wt.% Ni [43]. We remark that the loops of Fig. 12 display a

16

tendency to approach such a value at T = 5 K. The measurements suggest that the fraction of paramagnetic Ni ions with respect to the ferromagnetic-like fraction is larger in NiA derived NCs than in NiX-derived ones, because of the different morphology of these hosting materials at the mesoscale evidenced by the reported electron microscopy analysis. In principle, a magnetic contribution from the NiO fraction should be considered also, nanoparticulate Ni oxides being typically characterized by a weak ferromagnetic response stemming from the nanoparticle surface superimposed to the basically antiferromagnetic behaviour of the nanoparticle core. However, comparison with the recent literature [(Yuko Ichiyanagi, Naoto Wakabayashi, Junichiro Yamazaki, Saori Yamada, Yoshihide Kimishima, Eriko Komatsu, Hiroyuki Tajima - Magnetic properties of NiO nanoparticles - Physica B 329–333 (2003) 862–863, Farrakh Shahzad, Kashif Nadeem, Julia Weber, Heinz Krenn and Peter Knoll - Magnetic behavior of NiO nanoparticles determined by SQUID magnetometry - Mater. Res. Express 4 (2017) 086102][] shows that in the present case the absolute value of both effects (surface ferromagnetism and core antiferromagnetism) is negligible with respect to the magnetic signal provided by the Ni^0 nanoparticles.

Commentato [u2]: 2 nuovi lavori nella bibliografia

3.5. Discussion

Two sets of NCs where obtained by thermal treatment of NiA and NiX zeolites with comparable content of nickel, as obtained by an ionic exchange procedure that was repeated (on purpose) 10 times with the A zeolite and 6 times with the X zeolite, due to the more difficult exchange of Na^+ ions with the former zeolite.

The TG analysis (Fig. 1), carried out under a flow of gas with same composition of the thermal treatment adopted to obtain the NCs, showed that the NiA sample was more thermally stable with respect to the NiX zeolite. The two temperatures of treatment (735 and 750 °C) were chosen based on TG analysis results, in order to ensure the zeolite collapse: all this notwithstanding, a certain amount of residual NiA phase was detected both Rietveld analysis and confirmed by N_2 adsorption at -196 °C.

17

During the thermal treatments under reducing atmosphere, NiA and NiX zeolites are known to undergo the following phenomena [18,19]:

1) Reduction of Ni^{2+} to Ni^0 (with a possible structural damage of the zeolite framework).

2) Migration of the newly formed Ni^0 atoms to form clusters located within the microporous cavities of the zeolite.

3) Migration of the newly formed Ni^0 atoms outside the zeolite cavities to form metallic particles at the outer surface of the zeolite grains.

4) Thermal collapse of the zeolite framework.

5) Possible formation of amorphous and other crystalline phases.

The aforementioned phenomena may occur either simultaneously or in different steps, but are surely affected by several parameters, among which the type of metal cation and of zeolite, the temperature and duration of the thermal treatment under reducing atmosphere are the most relevant ones.

Given the nickel content of the dehydrated NiA and NiX zeolites as determined by AAS (*i.e.* 15.0 and 14.4 wt. %, in NiA and NiX, respectively), the largest chemical difference between the two zeolites is their Si/Al ratio (1.00 and 1.23, respectively). All this notwithstanding, the QPA of the final NCs showed substantial differences in the two sets of NCs derived from NiA and NiX, respectively. In particular, the higher thermal stability of NiA led to a certain amount of residual zeolite in the final materials, which exhibited also a very different morphology upon TEM observation. More interestingly, with NiA-derived NCs a smaller amount of Ni^{2+} was actually reduced (with respect to NiX-derived NCs), remaining embedded mostly in the amorphous phase, which actually protected the cations from reduction. Simultaneously, a prominent spillover phenomenon occurred, as testified by the amount of H_2 consumed during the TPR analysis, and by the presence of the HNi_2 phase, occurring only in NiA-derived NCs, which likely renders this material a powerful catalyst for hydrogenation reactions [37].

The thermal treatment under reducing atmosphere of the NiX sample leads to materials with a peculiar morphology (hedgehod-like particles are observed in TEM micrographs), characterized by a disordered mesoporosity, the almost total absence of residual NiX zeolite (in agreement with TG analysis) and by the presence of the NiO phase, as well as by a TPR H_2 consumption showing that the spillover phenomenon is unlikely to occur in NCs obtained by using the NiX zeolite precursor instead of NiA.

The zeolite precursor indeed markedly affects the physico-chemical properties of the final NCs. According to the literature, reduction of Ni^{2+} in dehydrated NiA zeolite mainly concerns i) Ni^{2+} cations located in the 6- and 8-membered rings facing α-cage (at lower temperature) and ii) Ni^{2+} cations located in the sodalite cage (β-cage, at higher temperature). With NiX zeolite, three different Ni^{2+} species are usually found to undergo reduction, namely Ni^{2+} cations in the supercage having very low interaction with the zeolite, Ni^{2+} cations in the supercage having very high interaction with the zeolite and Ni^{2+} cations in the hexagonal prisms (D6R units) [44-47].

In practice, the reduction of Ni^{2+} cations in NiA zeolite is in some extent different from that in NiX zeolite since the molecules H_2 reach Ni^{2+} cations in zeolite NiA with larger difficulty than in NiX, owing to lower dimensions of the windows of A zeolite.

As a whole, literature results support our present findings, *i.e.* the overall higher thermal stability (under reducing atmosphere) and the lower extent of Ni^{2+} reduction of NiA zeolite. On the contrary, the spillover effect observed here has not been reported, so far.

The different location of Ni^{2+} cations in the NiA and NiX zeolites and the related different extent of their reduction accounts for the difference in the morphology of Ni^0 NPs and the magnetic behavior of the NCs obtained from the two zeolites. As far as the morphology of Ni^0 NPs is concerned, it was found that Ni^0 NPs obtained from zeolite NiA exhibit a broader distribution and a larger average dimension with respect to those obtained from NiX zeolite. This finding could be explained by considering that Ni^{2+} cations in the supercage of NiX are more distant from each other with respect to Ni^{2+} cations located in the 6- and 8-membered rings facing α-cage in dehydrated NiA. Thus, the

19

growth of larger Ni^0 NPs, with a consequent broader size distribution, appears easier to occur in the reduction of Ni^{2+} cations of NiA, owing the shorter distance that the newly formed Ni^0 atoms have to cover to agglomerate in Ni^0 NPs, than in in the reduction of Ni^{2+} cations of zeolite Ni-X.

It should be also said that reduction of Ni^{2+} cations both in the sodalite cage (β-cage) of NiA and in the hexagonal prisms (D6R units) of NiX appears unlikely, considering that some Ni^{2+} cations are not reduced (Table 1) and that the reduction of Ni^{2+} cations in cavities with small windows, hampering the diffusion of the reducing agent, is more difficult.

As far as the NCs magnetic behavior is concerned, it is in good agreement with their morphology as determined by TEM analysis. It was found that NiX-derived NCs exhibit higher magnetization of saturation and lower coercivity than those obtained from NiA zeolite. Moreover, Ni^0 NPs of NiX-derived NCs magnetically interact more weakly than those obtained from NiA zeolite. These findings can be explained by considering that a higher magnetization of saturation is related to a higher amount of ferromagnetic Ni^0 NPs (which occur in NiX-derived NCs, as reported in Table 1) and a higher coercivity and magnetic interaction between NPs is related to a higher amount of paramagnetic, (unreduced) Ni^{2+} cations, which occur in NiA-derived NCs.

The extent to which the temperature and the duration of the thermal treatment under reducing atmosphere affect the morphology of the final products may be evaluated by examining the features NiA-derived NCs. The dimensions of Ni^0 NPs occurring in NiA735C-12min, NiA750C-12min and NiA750C-0min samples are in the range of 5-40 nm (average diameter = 17.6 nm), 10-45 nm (average diameter = 22.1 nm) and 5-30 nm (average diameter = 16.7 nm), respectively. Inspection of such data allows inferring that a higher temperature and a longer duration of the thermal treatment under reducing atmosphere favor a broader distribution of Ni^0 NPs dimension as well as a larger average dimension. Indeed, higher temperatures favor atoms mobility and longer times favor crystalline growth, finally leading to the formation of larger and less mono-dispersed Ni^0 NPs.

This last observation leads to the following considerations. For most of applications, the control of particles dimension and distribution is a crucial issue: by means of the here reported method, this

20

goal could be attained by properly selecting the zeolite precursor (*e.g.* zeolite framework, exchange capacity, Si/Al ratio), the exchange procedure, the metal content and the thermal treatment conditions (temperature, time and heating/cooling rate). Through a proper modulation of these parameters, the properties of the final NCs can be tailored to comply with a specific application.

Indeed, the method could be extended to other metal ions or even metal ions pairs allowing to obtain NCs characterized by a variable chemical composition for a wider range of applications. Therefore, the method here adopted has room for being further implemented and optimized, also considering that the NCs of this work were produced in tubular laboratory furnace in which a thin flow of a 2 % vol. H_2/Ar mixture lapped Ni-exchanged zeolite crystals kept in a small platinum vessel. Thus, it appears likely that Ni^{2+} reduction could be hindered by the poor contact between the reducing gas and the zeolite crystals. This last consideration suggests that the process subject of this work could attain better results if performed in a furnace ensuring a more intimate contact between the reducing gaseous stream and the crystals of zeolite, such as a fluidized bed reactor.

The method reported here is indeed smart, being based on two simple operations (ionic exchange and thermal treatment), versatile and (very likely) scalable.

4. CONCLUSIONS

In this work two types of Ni^{2+} exchanged zeolites (NiA and NiX) were used to prepare magnetic metal-ceramic nanocomposites by thermal treatments at relatively mild temperature under reducing atmosphere. This simple process results to be highly tunable in so far as the chemical composition, the structure and texture and macroscopic properties of the nanocomposites can be driven by the preparation parameters.

This process, which was already advantageously practiced to produce magnetic metal iron-ceramic nanocomposites used for DNA separation and pesticides removal from water [48,49], exhibits large potential for practical applications as it implies the use of low cost precursors (*i.e.* commercial zeolites).

21

However, there is another point that renders this process even more attractive. The review of the techniques of production of magnetic metal-ceramic nanocomposites, reported in the Introduction, evidenced that one of their drawbacks is that they give good results when performed on a laboratory scale, but are not suitable for larger scale production.

It appears at least peculiar that this smart process, if practiced on an industrial scale, seems to promise results even better than those, already very good [48,49], obtained on a laboratory scale. This statement is supported by the fact that the use of a fluidized bed reactor, which allows a very intimate contact between the reducing gas and the zeolite crystals, would be very reasonable at an industrial level. Moreover, performing at this level the reduction of heavy metal cation exchanged zeolites by a fluidized bed reactor would avoid some other limitations to which our rudimentary laboratory furnace is subjected. In particular, this furnace does not tolerate heating rates higher than 15 °C min^{-1} and needs, for safety reasons, to be operated with 2% vol. H_2/Ar mixture in order to avoid the risk of explosion. The adoption of faster heating and cooling rates and of a more powerful reducing agent, which appears possible at an industrial level, would still improve the results of this innovative process.

Electronic Supplementary Material: XRD pattern of parent A and X zeolites and of NiA and NiX samples are compared. N_2 adsorption isotherms at -196 °C of all prepared nanocomposites are shown. TEM and HR-TEM of samples NiA750-12min, NiX750-12min and NiA750-0min are reported

22

REFERENCES

[1] A.H. Lu, E.L. Salabas, F. Schut, Magnetic Nanoparticles: synthesis, protection, functionalisation, and application Angew. Chem., Int. Ed. 46 (2007) 1222-1244.

[2] S. Berensmeier, S. Magnetic particles for the separation and purification of nucleic acids, Appl. Microbiol. Biotechnol. 73 (2006) 495-504.

[3] I.J. Bruce, J. Taylor, M. Todd, M.J. Davies, E. Borioni, C. Sangregorio, T. Sen, Synthesis, characterization and application of silica-magnetite nanocomposite, J. Magn. Magn. Mater. 284 (2004) 145-160.

[4] S. Chikazumi, S. Taketomi, M. Ukita, M. Mizukami, H. Miyajima, M. Setogawa, Y. Kurihara, Physics of magnetic fluids, J. Magn. Magn. Mater. 65 (1987) 245-251.

[5] Lu, A.-H.; Schmidt, W.; Matoussevitch, N.; Bonnermann, H.; Spliethoff, B.; Tesche, B.; Bill, E.; Kiefer, W.; Schut, F. Nanoengineering of a Magnetically Separable Hydrogenation Catalyst, Angew. Chem. Int. Ed. 43 (**2004**) 4303- 4306.

[6] S.C.Tsang, V. Caps, I. Paraskevas, D. Chadwick, D. Thompsett, Magnetically separable, carbon-supported nanocatalysts for the manufacture of fine chemicals, Angew. Chem. Int. Ed., 43 (2004) 5645-5649.

23

[7] A.K.Gupta,M. Gupta, Synthesis and surface engineering of iron oxide nanoparticles for biomedical applications, Biomaterials 26 (2005) 3995-4021.

[8] S. Mornet, S. Vasseur, F. Grasset, P. Verveka, G. Goglio, A. Demourges, J. Portier, E. Pollert, E. Duguet, Magnetic nanoparticle design for medical applications, Prog. Solid State Chem. 34 (2006) 237-247.

[9] Z. Li, L. Wei, M.J. Gao, H. Lei, One-pot reaction to synthesize biocompatible magnetite nanoparticles, Adv. Mat. 17 (2005) 1001-1005.

[10] T. Hyeon, Chemical synthesis of magnetic nanoparticles, Chem. Comm. (2003) 927-934.

[11] D.W. Elliott, W.X. Zhang, Field assessment of nanoscale bimetallic particles for groundwater treatment, Environ. Sci. Technol. 35 (2001) 4922-4926.

[12] M. Takafuji, S. Ide, H. Ihara, Z. Xu, Preparation of poly(1-vinylimidazole)-grafted magnetic nanoparticles and their application for removal of metal ions, Chem. Mater.16 (2004) 1977-1983.

[13] I. M. Hsing, Y. Zhao, W. Zhao, Micro and nano magnetic particles for applications in biosensing, Electroanal.Electroanal. 19 (2007) 755-768.

[14] J. Gao, H. Gu, *Acc.* Multifunctional magnetic nanoparticles: design, synthesis and biomedical applications, Chem. Res. 42 (2009) 1097-1107.

[15] P. Tartaj, M. del Puerto Morales, S. Veintemillas-Verdaguer, T. Gonzalez-Carreno, C.J. Serna, The Preparation of magnetic nanoparticles for applications in biomedicine, J. Phys. D: Appl. Phys. 36 (2003) 182-197.

[16] S. Esposito, A. Marocco, B. Bonelli, M. Pansini, Produzione di materiali compositi metallo-ceramici nano strutturati da precursori zeolitici. Brevetto Italiano, n. MI 2014 A 000522.

[17] S. Esposito, A. Marocco, B. Bonelli, M. Pansini, Production of magnetic metal nanoparticles embedded in a silica-alumina matrix, PCT International Application Published under Number WO 2015/145230 A1.

[18] D.W. Breck, Zeolite Molecular Sieves: Structure, Chemistry and Uses, Wiley, New York, 1974.

[19] F.G. Dwyer, An Introduction to Molecular Sieves Zeolites, J. Wiley and Sons, Chichester (UK), 1988.

[20] A. Marocco, G. Dell'Agli, S. Esposito, M. Pansini, Metal-ceramic composite materials from zeolite precursor, Solid State Science 14 (2012) 394-400.

[21] S. Ronchetti, E.A. Turcato, A. Delmastro, S. Esposito, C. Ferone, M. Pansini, B. Onida, D. Mazza, Study of the thermal transformations of Co- and Fe-exchanged zeolites A and X by "in situ" XRD under reducing atmosphere, Mater. Res. Bull. 45 (2010) 744-750.

[22] A. Marocco, G. Dell'Agli, S.Esposito, M. Pansini, Parameters expediting the thermal conversion of Ba-exchanged zeolite A in monoclinic celsian, Advances in Materials Science and Engineering (2010) Article ID 683429, 8 pages, doi:10.1155/2010/683429.

25

[23] A. Marocco, G. Dell'Agli, S. Esposito, M. Pansini, The role of the residual Na^+ and Li^+ on thermal transformations of Ba-exchanged zeolite A, Solid State Sciences 13 (2011) 1143-1151.

[24] F. Sannino, S. Ruocco, A. Marocco, S. Esposito, M. Pansini, Cyclic process of simazine removal from waters by adsorption on zeolite H-Y and its regeneration by thermal treatment, J. Hazard. Mat. 229-230 (2012) 354-360.

[25] F. Sannino, S. Ruocco, A. Marocco, S. Esposito, M. Pansini, Simazine removal from waters by adsorption on porous silica tailored by sol-gel technique, Micropor. Mesopor. Mat. 180 (2013) 178-186.

[26] A. Marocco, G. Dell'Agli, B. Liguori M. Pansini, Sintering behaviour of celsian based ceramics obtained from the thermal conversion of (Ba, Sr)-exchanged zeolite, J. Eur. Ceram. Soc. 31 (2011) 1965-1973.

[27] S. Esposito, A. Marocco, G. Dell'Agli, B. de Gennaro, M. Pansini, Relationships between the water content of zeolites and their cation population, Micropor.Mesopor. Mat. 202 (2015) 36-43.

[28] C. Ferone, B. Liguori, A. Marocco, S. Anaclerio, M. Pansini, C. Colella, Monoclinic (Ba, Sr)-celsian by thermal treatment of (Ba, Sr)-exchanged zeolite A, Micropor. Mesopor. Mat. 134 (2010) 65-71.

[29] R.Cioffi, M. Pansini, D. Caputo, C. Colella, Evaluation of mechanical and leaching properties of cement-based solidified materials encapsulating Cd-exchanged natural zeolites, Env. Tech. 17 (1996) 1215-1224.

26

[30] A.F. Gualtieri, E. Mazzucato, P. Venturelli, A. Viani, P. Zannini, L. Petras, X-ray powder diffraction quantitative analysis performed in situ at high temperature: application to the determination of NiO in ceramic pigments, J. Appl. Crystallogr. 32 (1999) 808-813.

[31] A.C.Larson, R.B. Von Dreele, General structure analysis system ″GSAS″; Los Alamos National Laboratory Report; Los Alamos, LAUR (1994) 86-748.

[32] B.H. Toby, EXPGUI, a Graphical user interface for GSAS, J. Appl. Crystallogr. 34 (2001) 210−213.

[33] F. Rouquerol, J. Rouquerol, Adsorption by powders and porous solids: principles methodology and application, K. Sing, Academic Press, London, 1999.

[34] B. Coughlan, W.M. Carroll, W.A. McCann, On the crystal stability of outgassed NiA zeolite, Proceedings of the Royal Irish Academy 76 (1976) 349-358.

[35] S. Akbar, K. Dad, T.H. Shah, R.J. Shahnaz, The determination of zeolitic water and thermal stability of Nickel exchanged X-zeolites by TGA and DTA, Chem. Soc. Pak. 28 (2006) 317-322.

[36] Y.P. Khodyrev, R.V. Baranova, R.M. Imamov, S.A. Semiletov, Electron diffraction investigation of hexagonal nickel hydride, Kristallografiya 23 (1978) 724-728.

[37] A.G. Boudjahem, M.M. Bettahar, Effect of Oxidative pre-treatment on hydrogen spillover for a Ni/SiO$_2$ catalyst, J. Mol. Catal. A-Chem. 426 (2017) 190-197.

[38] D.J. Čejka, H. van Bekkum, A. Corma, F. Schüth, Studies in Surface Science and Catalysis: Introduction to Zeolite Molecular Sieves, Elsevier, Amsterdam, 2007.

[39] P. Allia, G. Barrera, P. Tiberto, T. Nardi, Y. Leterrier, M. Sangermano, Fe_3O_4 nanoparticles and nanocomposites with potential application in biomedicine and in communication technologies: nanoparticle aggregation, interaction, and effective magnetic anisotropy, J. Appl. Phys. 116 (2014) 113903-1 - 113903-9.

[40] W.J. Jr. Carr, Temperature dependence of ferromagnetic anisotropy, Phys. Rev., 9 (1958) 1971-1976.

[41] A.C. Scheinhost, R.G. Ford, D.L. Sparks, The role of Al in the formation of secondary Ni precipitates on pyrophyllite, gibbsite, talc, and amorphous silica: a DRS study, Geochim. Cosmochim. Acta 63 (1999) 3193–3203.

[42] A.N. Mlinar, G.B. Baur G.G. Bong, A. Getsoian, A.T. Bell, Propene oligomerization over Ni-exchanged Na-X zeolites J. Catal. 296 (2012) 156–164.

[43] B.D. Cullity, C.D. Graham, Introduction to Magnetic Materials, Wiley, Hoboken, 2009.

[44] P. Gallezot, B. Imelik, Location of nickel ions in zeolite Y. Influence of thermal treatment and exchange level on nickel positions, J. Phys. Chem. 77 (1973) 652-656.

[45] R. Bhat, P.B. Gangundi, A.N. Bhat, Nickel ion-exchanged zeolite 4A: reduction behavior and structure stability, J. Chem. Soc. Farad. Trans. 91 (1995) 3983-3986.

[46] M. Suzuki, K. Tsutsumi, K. Takahashi, Characterization and catalytic activity of nickel-zeolite catalysts. I. Reduction properties of nickel ions in zeolites, Zeol. 2 (1982) 51-58.

[47] A. Luengnaruemitchai, A. Kaengsilalai, Activity of different zeolite-supported catalysts for methane reforming with carbon dioxide, Chem. Eng. J. 144 (2008) 96-102.

[48] M. Pansini, G. Dell'Agli, A. Marocco, P.A. Netti, E. Battista, V. Lettera, P. Vergara, P. Allia, B. Bonelli, P. Tiberto, G. Barrera, G. Martra, R. Arletti, S. Esposito, Preparation and characterization of magnetic and porous metal-ceramic nanocomposites from a zeolite precursor and their application for DNA separation, J. Biomed. Nanotech 13 (2018) 337-348.

[49] M. Pansini, F. Sannino, A. Marocco, P. Allia, P. Tiberto, G. Barrera, M. Polisi, E. Battista, P.A. Netti, S. Esposito, Novel process to prepare magnetic metal-ceramic nanocomposites from zeolite precursor and their use as adsorbent of agrochemicals from water, J. Env. Chem. Eng. 6 (2018) 527–538.

Table 1. Results of quantitative phase analyses as obtained by RIR-Rietveld refinements (wt. % with standard errors in brackets)

Sample	Ni-A	N-Xi	Ni^0	Cristobalite	NiO nanophase	HNi_2	Amorphous phase %
NiA735C-12min	5.2(2)		7.4(1)	traces	0.8(2)	0.7(2)	85.9
NiA750C- 12min	2.4(2)		4.0(1)			4.1(1)	89.5
NiA750C- 0min	8.5(2)		6.4(5)	traces	1.4(2)	0.7(2)	83.0
NiX735C-12min		0.3(1)	9.7(1)		5.3(4)		84.7
NiX750C- 12min		0.3(2)	10.3(1)		5.7(3)		83.7
NiX750C- 0min		0.3(1)	9.6(1)		5.7(3)		84.4

Table 2. Specific surface area (S_{BET}), total pore volume (V_p), micropore volume (V_{mp})as obtained by N_2 isotherms at -196 °C

Sample	S_{BET} (m^2g^{-1})	$V_p(cm^3 g^{-1})$	$V_{mp}(cm^3g^{-1})$[a]
NiA735C-12min	9	0.021	2.7×10^{-3}
NiX735C-12min	27	0.097	0
NiA750C-12min	6	0.028	3.5×10^{-3}
NiX750C-12min	10	0.037	0
NiA750C-0min	19	0.058	5×10^{-3}
NiX750C-0min	36	0.11	1.1×10^{-3}

Captions to Figures

Fig. 1. DTA (grey curve) and TG-DTG curves (black lines) of (a) NiA and (b) NiX samples, as obtained under 2 vol. % H_2 in Ar atmosphere in the 30-850 °C temperature range.

Fig. 2. Observed (black cross) and calculated (red line) diffraction patters and final difference curve (purple line) from Rietveld refinements of the samples NiA735C-12min (a), NiA750C-12min (b) and NiA750C-0min (c). Tick marks are relative to the different phases: black: Al_2O_3 standard; blue: LTA; green: metallic Ni; red: nickel hydride; yellow: bunsenite.

Fig. 3. Observed (black cross) and calculated (red line) diffraction patters and final difference curve (purple line) from Rietveld refinements of the samples NiX735C-12min (a), NiX750C-12min (b) and NiX750C-0min (c). Tick marks are relative to the different phases: black: Al_2O_3 standard; blue: metallic Ni; green: zeolite X; red: bunsenite.

Fig. 4. Pore size distribution of the samples (a) NiA735C-12min and NiX735-12min, (b)NiA750C-0min and NiX750-0minand (c) NiA750C-12min and NiX750-12min as obtained by applyingthe NL-DFT method.

Fig. 5. TEM (sections a and b) and HR-TEM (section c) images collected on the NiA735C-12min material. Profile reporting the distance among the fringes observed on the particle signalled by the dashed harrow in section c and Fourier Transform of the same image (section d). Instrumental magnification: 6000×, 30000× and 400000×.

31

Fig. 6. TEM (sections a, b and c) and HR-TEM (section d) images collected on the NiA750C-0min material. Profile reporting the distance among the fringes observed on the particle signalled by the dashed harrow in section d and Fourier Transformed of the same image (section e). Instrumental magnification: 8000×, 30000×, 100000× and 400000×.

Fig. 7. TEM (sections a and b) and HR-TEM (section c) images collected on the NiX735C-12min material. The profiles reporting the distance among the fringes observed on the particles signalled by the dashed harrow in section d are also reported. Instrumental magnification: 4000×, 100000× and 400000×.

Fig. 8. Ni particle size distributions of the synthesized materials. Upper right panel: the distribution of nanoparticle diameters in sample NiX735C-12 min as obtained from FC/ZFC curves is superimposed to the histogram (see text for details). **<Nuova Figura 8: si trova in fondo a questo documento>**

Fig. 9. a) Room-temperature (T = 300 K) saturation magnetization M_s of nanocomposites obtained from Ni-loaded A/X zeolites. B): plot of M_s as a function of the total content of metallic Nickel and hexagonal nickel hydride (data taken from Table 1).

Fig. 10. Room-temperature (T = 300 K) coercive field of nanocomposites obtained from Ni-loaded A/X zeolites.

Fig. 11. FC/ZFC curves under a field of 200 Oe for nanocomposites obtained from two Ni-loaded A/X zeolites.
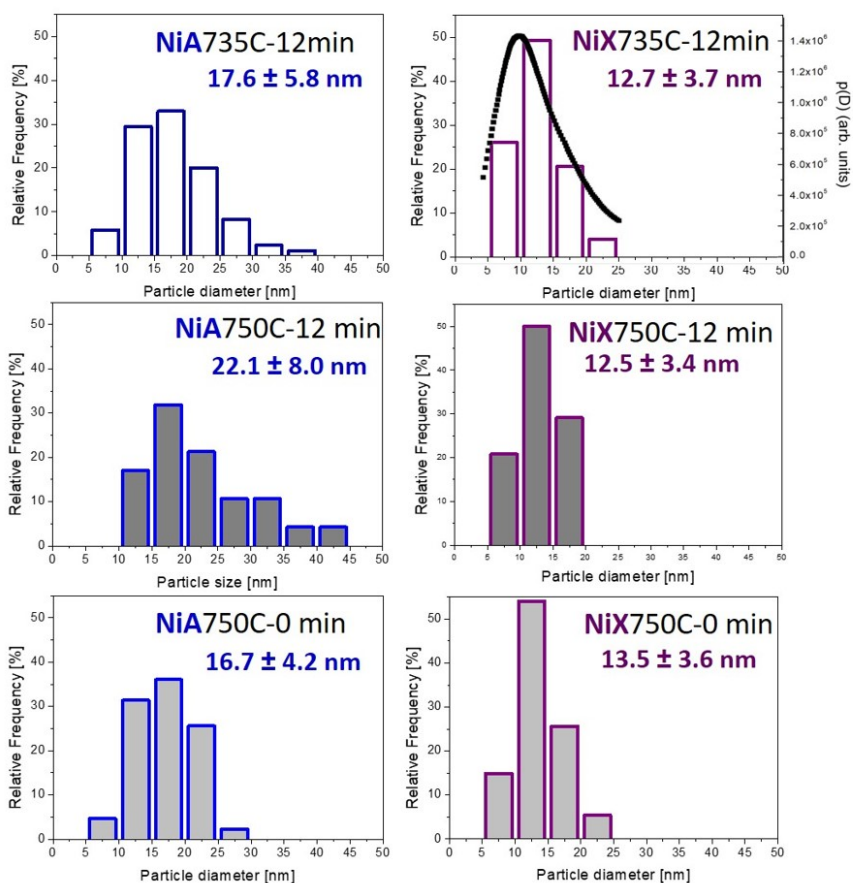
Fig. 12. M(H) loops of two nanocomposites obtained from Ni-loaded A/X zeolites at 5 K (black symbols) and at room temperature (red symbols). Inset in bottom panel: experimental M(H) curve (open symbols) and single-moment Langevin function (full blue line) in sample NiX735C-12min at room temperature. The best-fit magnetic moment in the Langevin function is $\mu = 3.29 \times 10^{-16}$ emu.
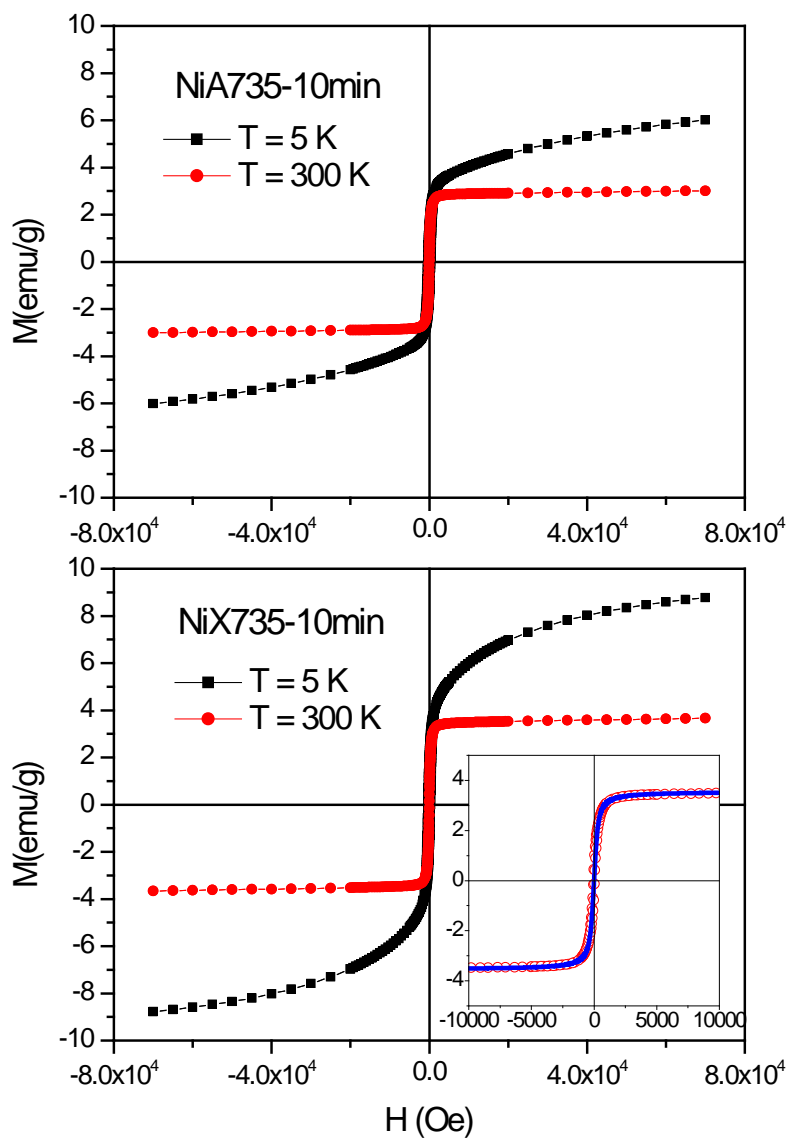
<NuovaFigura 12: si trova in fondo a questo documento>

Fig. 13. Experimental M(H) curve (open symbols) and single-moment Langevin function (full red line) in sample NiX735C-12min at room temperature. <Figura eliminata e fusa con la 12>

Fig. 14. Distribution of nanoparticle diameters in sample NiX735C-12 min as obtained from FC/ZFC curve analysis (full symbols) and from TEM image analysis (hystogram; see Fig. 7). <Figura eliminata e fusa con la 8>

<NuovaFig. 8>

<NuovaFig. 12>